



HAL
open science

Carbon Nanotube Degradation in Macrophages: Live Nanoscale Monitoring and Understanding of Biological Pathway

Dan Elgrabli, Walid Dachraoui, Cécilia Ménard-Moyon, Xiao Jie Liu, Dominique Begin, Sylvie Bégin-Colin, Alberto Bianco, Florence Gazeau, Damien Alloyeau

► **To cite this version:**

Dan Elgrabli, Walid Dachraoui, Cécilia Ménard-Moyon, Xiao Jie Liu, Dominique Begin, et al.. Carbon Nanotube Degradation in Macrophages: Live Nanoscale Monitoring and Understanding of Biological Pathway. ACS Nano, 2015, 9 (10), pp.10113-10124. 10.1021/acsnano.5b03708 . hal-02557774

HAL Id: hal-02557774

<https://hal.science/hal-02557774>

Submitted on 9 Nov 2023

HAL is a multi-disciplinary open access archive for the deposit and dissemination of scientific research documents, whether they are published or not. The documents may come from teaching and research institutions in France or abroad, or from public or private research centers.

L'archive ouverte pluridisciplinaire **HAL**, est destinée au dépôt et à la diffusion de documents scientifiques de niveau recherche, publiés ou non, émanant des établissements d'enseignement et de recherche français ou étrangers, des laboratoires publics ou privés.

This document is confidential and is proprietary to the American Chemical Society and its authors. Do not copy or disclose without written permission. If you have received this item in error, notify the sender and delete all copies.

Carbon nanotube degradation in macrophages: live nanoscale monitoring and understanding of biological pathway

Journal:	<i>ACS Nano</i>
Manuscript ID:	nn-2015-03708r.R1
Manuscript Type:	Article
Date Submitted by the Author:	n/a
Complete List of Authors:	Elgrabli, Daan; Université paris 7, MSC dachraoui, walid; Université Paris 7 Denis Diderot, MPQ Ménard-Moyon, Cécilia; CNRS, UPR9021, ICT Liu, Xiao Jie; Université de Strasbourg, Begin, Dominique; CNRS, Begin-Colin, Sylvie; Université de Strasbourg, Bianco, Alberto; CNRS, UPR3572, Immunopathologie et Chimie Thérapeutiques Gazeau, Florence; Université Paris-Diderot, Batiment Condorcet Alloyeau, Damien; Université Paris 7 Denis Diderot, Laboratoire Matériaux et Phénomènes Quantiques

SCHOLARONE™
Manuscripts

1
2
3
4
5
6
7
8
9
10
11
12
13
14
15
16
17
18
19
20
21
22
23
24
25
26
27
28
29
30
31
32
33
34
35
36
37
38
39
40
41
42
43
44
45
46
47
48
49
50
51
52
53
54
55
56
57
58
59
60

Carbon Nanotube Degradation in Macrophages: Live Nanoscale Monitoring and Understanding of Biological Pathway

*Dan Elgrabli^{1‡}, Walid Dachraoui^{2‡}, Cécilia Ménard-Moyon³, Xiao Jie Liu⁴, Dominique Bégin⁴,
Sylvie Bégin⁵, Alberto Bianco³, Florence Gazeau^{1*} and Damien Alloyeau^{2*}*

(1) Laboratoire Matière et Systèmes Complexes, UMR7057 CNRS/Université Paris Diderot,
Paris France.

(2) Laboratoire Matériaux et Phénomènes Quantiques, UMR7057 CNRS/Université Paris
Diderot, Paris France.

(3) CNRS, Institut de Biologie Moléculaire et Cellulaire, Laboratoire d'Immunopathologie et
Chimie Thérapeutique, 67000 Strasbourg, France

(4) Institut de Chimie et des Procédés pour L'Energie, l'Environnement et la Santé (ICPEES)
UMR 7515, Université de Strasbourg, 25 rue Becquerel, 67087 Strasbourg cedex 2 France

(5) Institut de Physique et de Chimie de Strasbourg (IPCMS) UMR 7504 CNRS-Université de
Strasbourg, 23 rue du Loess, BP 34 67034 Strasbourg cedex 2, France

1
2
3
4
5
6
7
8
9
10
11
12
13
14
15
16
17
18
19
20
21
22
23
24
25
26
27
28
29
30
31
32
33
34
35
36
37
38
39
40
41
42
43
44
45
46
47
48
49
50
51
52
53
54
55
56
57
58
59
60
KEYWORDS

Biodegradation, Carbon nanotubes, macrophages, genetic response, liquid-cell transmission electron microscopy, reactive oxygen species.

ABSTRACT

Despite numerous applications, the cellular-clearance mechanism of multi-walled carbon nanotubes (MWCNTs) has not been clearly established yet. Previous *in vitro* studies showed the ability of oxidative enzymes to induce nanotube degradation. Interestingly, these enzymes have the common capacity to produce reactive oxygen species (ROS). Here, we combined material and life science approaches for revealing an intra-cellular way taken by macrophages to degrade carbon nanotubes. We report the *in situ* monitoring of ROS-mediated-MWCNT degradation by liquid-cell transmission electron microscopy. Two degradation mechanisms induced by hydroxyl radicals were extracted from these unseen dynamic nanoscale investigations: a non-site-specific thinning process of the walls and a site-specific transversal drilling process on pre-existing defects of nanotubes. Remarkably, similar ROS-induced structural injuries were observed on MWCNTs after aging into macrophages from one to seven days. Beside unraveling oxidative transformations of MWCNT structure, we elucidated an important, albeit not exclusive, biological pathway for MWCNT degradation in macrophages, involving NOX₂ complex activation, superoxide production and hydroxyl radical attack, which highlights the critical role of oxidative stress in cellular processing of MWCNTs.

1
2
3
4
5
6 Although carbon nanotubes (CNTs) are one of the most promising nanomaterials for technological
7
8 and pharmaceutical applications,^{1, 2} many grey areas remain on their life cycle in biological
9
10 environments, notably regarding their biodegradation mechanisms that drastically impact their
11
12 efficiency and innocuousness. In the last years, a few studies have investigated CNT biokinetics
13
14 (translocation, biodistribution and clearance) *in vivo*,³⁻⁵ revealing that, like most nanomaterials,
15
16 their “journey” in the organism mainly ends in macrophage cells in lung after intratracheal
17
18 instillation,^{3, 6} or in liver and spleen after intravenous injection.^{7, 8} A slow degradation of CNTs
19
20 seems to occur in phagosomes,^{3, 9} but the biochemical and structural processes involved in the
21
22 degradation of graphitic nanostructures remain unclear. *In vitro* enzymatic biodegradation of
23
24 CNTs have shown that horseradish peroxidase (HRP), an enzyme from plant, can oxidize single-
25
26 walled CNTs (SWCNTs) in the presence of low levels of hydrogen peroxide.¹⁰ CNT
27
28 biodegradation studies were then extended to other peroxidases such as myeloperoxidase (MPO)¹¹
29
30 present in neutrophils, eosinophil peroxidase (EPO)¹² and lactoperoxidase (LPO)¹³ expressed by
31
32 goblet cells found in the epithelial lining of the respiratory tract as well as in many human exocrine
33
34 secretions. The degradation mechanisms rely on the ability of MPO, EPO and LPO to convert
35
36 hydrogen peroxide (H₂O₂) into hypochlorous, hypobromous and hypothiocyanous acids,
37
38 respectively. As observed for microorganisms, SWCNTs can be entrapped by a network of
39
40 chromatin and proteins outside the cells and undergo acellular MPO-mediated biodegradation.¹⁴
41
42 In the same way, non-enzymatic degradation medium constituted by phagosolysosomal elements
43
44 associated with H₂O₂ is also able to degrade CNTs.¹⁵ All these results emphasize the capacity of
45
46 oxidant species to induce CNT degradation.. Kagan and coworkers have recently demonstrated the
47
48 ability of lung macrophages to degrade CNTs in extra-cellular fluid using superoxide/Peroxynitrite
49
50
51
52
53
54
55
56
57
58
59
60

1
2
3 oxidative pathways.¹⁶ Here, we combined materials sciences and biological approaches to reveal
4 another way taken by macrophages to degrade functionalized multi-walled carbon nanotubes
5 (MWCNTs) in intra-cellular compartments, which also involves the oxidizing power of reactive
6 oxygen species (ROS) produced by an enzymatic complex. On the one hand, *in situ* transmission
7 electron microscopy (TEM) in liquid provided an unprecedented live monitoring of the ROS-
8 induced damages in MWCNT structure. On the other hand molecular and chemical biology
9 highlighted the crucial role of NADPH oxidase 2 (NOX₂) enzymatic complexes in the ROS-
10 production mechanisms responsible for MWCNT degradation.
11
12
13
14
15
16
17
18
19
20
21
22

23 **Results and discussion**

24 **Structural degradation of MWCNTs induced by ROS in macrophages.**

25
26
27 We carried out TEM analyses of the structural degradation of MWCNTs as a function of their
28 aging time (t_{ag}) in THP-1 cells differentiated into macrophages. These studies were performed with
29 two types of nanomaterials: MWCNTs and MWCNTs filled with magnetic iron oxide
30 nanoparticles (namely Fe@MWCNTs). These latter were synthesized with a high-yield two-step
31 process.¹⁷ In both cases, MWCNTs were functionalized by arylation to introduce amino groups on
32 the nanotube sidewall and to ensure a good dispersion in physiological media. In view of
33 cytotoxicity assessments after 24h exposure to CNTs (Figure S1), we choose a dose of MWCNTs
34 and Fe@MWCNTs of 5 $\mu\text{g/ml}$ inducing a cell-death degree below 5%. After t_{ag} of 3h, 24h, 48h
35 and 168h, CNTs were extracted from cells to perform TEM observations. As can be seen in Figure
36 1a for MWCNTs and Figure S2 for Fe@MWCNTs, the graphitic nanostructures are deeply scarred
37 by cells. The main stigmata of degradation processes are the presence of holes in the carbon walls.
38 High resolution TEM allows confirming that these holes can be either drilled through one side or
39
40
41
42
43
44
45
46
47
48
49
50
51
52
53
54
55
56
57
58
59
60

1
2
3 through the whole nanotube structure (Figure S3a-c). The t_{ag} -dependent analyses of the percentage
4 of perforated area (P_a , Figure 1b), the average surface area of holes (\bar{S} , Figure 1c) and the number
5 of holes per surface unit (D , Figure 1d) provide a better overview of the degradation mechanisms.
6
7
8
9
10 The degradation of MWCNTs quickly increases over time in cells, with P_a reaching 51 % after
11 168 h aging. However, the 25-fold increase of P_a when increasing t_{ag} from 3h to 168h is
12
13 concomitantly due to the raise of \bar{S} and D , that vary as $t^{1/3}$ and $t^{1/2}$, respectively. As $P_a = \bar{S} \times D$,
14
15 our measurements allows evaluating the respective weight of the nucleation and growth of holes
16
17 on the expansion of structural damage in MWCNTs. The fast increase of D , yet slowed down by
18
19 the coalescence of holes, reveals that MWCNTs present many energetically-affordable onset of
20
21 degradation and indicates that the degradation mechanisms are not dominated by the expansion of
22
23 holes drilled on sparse preferential sites. We also noted that the mean thickness of the nanotube
24
25 walls was reduced by 15% after 168h in macrophages. Figure 1e shows that the amount of ROS
26
27 quantified by 2',7'-dichlorodihydrofluorescein diacetate (DCFDA) is approximatively 3-fold
28
29 increased when MWCNTs or Fe@MWCNTs are incubated 24h with THP-1-derived macrophages.
30
31 This enhanced production of ROS is in agreement with previous studies on other macrophages¹⁸
32
33 and it highlights the possible role of these highly oxidative species in the degradation of exogenous
34
35 nanomaterials.^{11, 19, 20} In order to test this hypothesis, we assessed the effects of N-acetyl-L-
36
37 cysteine (NAC), a ROS scavenger inducer, on degradation of MWCNTs. NAC significantly
38
39 reduced the cellular production of ROS, which was still 20% higher than the untreated control
40
41 (Figure 1e). Interestingly, the presence of NAC substantially prevented the degradation of both
42
43 MWCNTs and Fe@MWCNTs. Up to 3-fold decrease of P_a was measured after 48h intracellular
44
45 aging in the presence of NAC, while both \bar{S} and D were also reduced (Figure 1b-d). This confirms
46
47 that antioxidant inducers diminish both nucleation and growth of cell-induced damages in
48
49
50
51
52
53
54
55
56
57
58
59
60

1
2
3 MWCNTs. The kinetics and mechanisms of degradation of Fe@MWCNTs are very similar to the
4
5 ones of MWCNTs, suggesting that iron embedded into nanotubes do not interplay with the
6
7 degradation mechanisms. The relevance of all these statistical measurements was validated by
8
9 Kolmogorov-Smirnov tests (Figure S4).
10
11

12
13 As these important alterations of the graphitic structures could also modify the cytotoxicity effects
14
15 of CNTs over time, we evaluated if the products of degradation extracted from cells 24h after
16
17 exposure are more or less toxic than the original forms. Using Alamar blue assay, we compared
18
19 the lethal dose inducing 50% cell death (LD50) for MWCNTs, Fe@MWCNTs and their
20
21 degradation products (namely dMWCNT and dFe@MWCNT respectively). Interestingly, Figure
22
23 S5 shows that the degradation products are less toxic (LD50 was 47.2 and 54.3 $\mu\text{g/ml}$ for
24
25 dMWCNT and dFe@MWCNT, respectively) than the original nanosystems (LD50 was 27.7
26
27 $\mu\text{g/ml}$ for both MWCNTs and Fe@MWCNT), revealing that cell processing of MWCNTs tends
28
29 to minimize their cytotoxicity.
30
31
32
33

34
35 Reducing the gap between *in vitro* and *in vivo* investigations is an essential prerequisite to fully
36
37 understand CNT lifecycle in the organism and to exploit this knowledge in biomedicine. As a first
38
39 step, we compared the degradations of graphitic structures in cell cultures and in animals. Rats
40
41 were exposed to MWCNTs *via* intra-tracheal instillation and *ex vivo* TEM analyses revealed the
42
43 presence of exogenous nanomaterials in macrophages of the lungs and the lymph nodes, 7 days
44
45 after the exposure (figure S6). However, by analysing closely these TEM experiments, we can
46
47 clearly observed the presence of many holes in the structure of the tubes. Therefore, these highly
48
49 perforated nanotubes indicate that the oxidative degradation processes analysed over time through
50
51 *in vitro* approach, are very similar to the structural alterations of CNTs occurring *in vivo*.
52
53
54
55
56
57
58
59
60

***In situ* nano-scale monitoring of the ROS-induced damages in MWCNTs.**

Liquid-cell TEM has provided the opportunity to follow nanoscale processes at the interfaces between liquids and solids, opening many avenues in both material and life sciences.^{21, 22} It is well-established that the electron-beam irradiation of water generates the following primary products by radiolysis: hydrated electrons (e_h^-), hydrogen radicals (H^\bullet), hydroxyl radicals (OH^\bullet), dihydrogen (H_2), H_2O_2 , hydronium ions (H_3O^+), hydroperoxyl radicals (HO_2^\bullet).²³ When nanoscale analyses are performed in water, these species are uniformly distributed within the irradiated region with concentrations varying as sub-linear power laws of the electron-dose rate (\dot{d}).²⁴ The straightforward control over the local production of strong reducing agent (e_h^- , H^\bullet) has been deeply exploited to study the nucleation and growth of metal nanoparticles *via* the reduction of metallic precursor.²⁵⁻²⁹ Here, we investigated the degradation mechanisms of MWCNTs and Fe@MWCNTs in water under electron beam irradiation and we identified the oxidizing species involved in this chemical attack. Structural modifications of MWCNTs was simultaneously generated and imaged in scanning transmission electron microscopy (STEM) mode at 80 kV. Signals were collected with a high annular angular dark field (HAADF) detector. The high signal-to-noise ratio of STEM-HAADF imaging, in which \dot{d} is proportional to the square of the magnification, allows distinguishing two mechanisms in the degradation of MWCNTs. Figure 2a illustrates that the cylindrical nanostructures sustain a wall-by-wall thinning until breaking of the tube. Interestingly, this erosion occurs all along the irradiated surfaces of CNTs. Intensity profiles measured perpendicularly to the anisotropy axis also reveals that both inner and outer sides of the MWCNTs are attacked, suggesting that chemical species are also generated inside the inner cavity when the electron beam pass through the nanotubes. This induces a reduction of the outer diameter

1
2
3 and an increase of the inner diameter that were measured to be linear with time (Figure 2b). By
4
5 defining the speed of thinning process as the slope of the linear relation of diameters and time, we
6
7 demonstrated that the kinetic of degradation is enhanced with \dot{d} . For example, the speed of
8
9 degradation for the outer diameter was boosted from 0.6 nm/s to 2.3 nm/s, when stepping up \dot{d}
10
11 from $3.4 \cdot 10^7 \text{ Gy}\cdot\text{s}^{-1}$ (magnification of 150k) to $2.4 \cdot 10^8 \text{ Gy}\cdot\text{s}^{-1}$ (magnification of 400k) (Figure 2c).
12
13 Together with this non-site-specific thinning, MWCNTs sometimes endure more severe damages
14
15 consisting in transversal drillings of the walls. Figure 3a shows that this second degradation
16
17 mechanism can either generate spherical holes if the drilling axis is almost perpendicular to the
18
19 tube axis or can tear the nanotubes lengthwise for more grazing drilling angles, pulling out together
20
21 many walls from the tubes and creating elongated holes. As these drilling processes were not
22
23 systematically observed, one can reasonably assume that pre-existing defects in the MWCNTs
24
25 (pentagon-hexagon pairs, atomic vacancies, dislocations, presence of functional groups that lead
26
27 to the formation of sp^3 hybridized carbon atoms, etc.), that are more reactive due to deformation,
28
29 may favor this faster degradation mechanisms. This assumption is strengthened by the degradation
30
31 mechanisms of Fe@MWCNTs that in rare cases present iron oxide nanoparticles inserted in
32
33 between the nanotubes walls (Figure 3b). As observed by *ex situ* HRTEM (Figure S7), the
34
35 MWCNT structure presents a high rate of crystalline defects in these interface areas. These highly-
36
37 reactive zones systematically serve as onset for transversal drilling by tearing along the interface
38
39 between the tube and the nanoparticles. Figure 3b (100 and 120 minutes of observation) also
40
41 illustrates that the degradation of the last remaining walls of nanotubes frequently occurs through
42
43 a slower wall-by-wall thinning. Although the encapsulated iron-oxide nanoparticles move inside
44
45 the MWCNTs under beam irradiation, their dispersion in the liquid cell is possible only after the
46
47
48
49
50
51
52
53
54
55
56
57
58
59
60

1
2
3 rupture of the tubes, illustrating the potential of biodegradable MWCNTs for drug delivery
4 applications.³⁰
5
6

7
8
9 It is worth to note that no structural alteration was observed when MWCNTs and Fe@MWCNTs
10 were irradiated for several hours with the same optical conditions under vacuum (Figure 4a). As
11 the energy of incident electrons was below the knock-on-damage threshold in MWCNTs, the
12 degradation processes observed in water are unambiguously induced by chemical reactions.
13
14 Furthermore, both wall-by-wall thinning and drilling mechanisms were exclusively observed in
15 the irradiated areas showing the short life-time and very low diffusion of the involved chemical
16 species. Schneider *et al.* have calculated that among the radiolysis products only the highly reactive
17 species (e_h^- , H^\bullet , OH^\bullet) are strictly restricted to the irradiated region. Thus, the strong oxidation
18 potential of OH^\bullet makes it the most likely candidate for the chemical degradation of MWCNTs.
19
20 The dose-dependent concentration of this short-lived ROS, that varies as $d^{0.46}$,²⁴ is also consistent
21 with the degradation boosting observed for higher magnifications. This damaging role of OH^\bullet was
22 definitely confirmed by the long-term stability of MWCNTs in ethanol (Figure 4b), in which
23 ionizing radiations generate peroxy radicals, but no OH^\bullet .³¹
24
25
26
27
28
29
30
31
32
33
34
35
36
37
38
39

40 Additionally, the two mechanisms of degradation extracted from these *in situ* TEM observations
41 are in agreement with previous spectroscopy studies that suggested two concomitant destructive
42 interactions of OH^\bullet with MWCNTs³²: 1) OH^\bullet could preferentially attack MWCNTs at the defect
43 sites to produce carboxylic acid groups leading to disordered and perforated walls. Note that, the
44 covalent functionalization by arylation induces the rehybridization of sp^2 carbon atoms to sp^3 , thus
45 increasing the amount of defects and the reactivity of the MWCNTs towards OH^\bullet in the vicinity
46 of the functionalized carbon atoms. 2) OH^\bullet could also insert a significant amount of hydroxyl
47 groups on unsaturated C=C bonds of the nanotube sidewalls by electrophilic addition reaction, that
48
49
50
51
52
53
54
55
56
57
58
59
60

1
2
3 are then converted into quinones and eventually carboxylic acids. MWCNT functionalization also
4
5 imparts enhanced hydroxyl radical capture ability, in particular OH^{\bullet} .³³⁻³⁵ Interestingly, the
6
7 presence of hydroxyl and carbonyl functions was detected on MWCNTs extracted from rat lung³.
8
9 These oxygen-containing functional groups emphasize on the putative role of OH^{\bullet} in MWCNT
10
11 degradation in cells. Although the dynamic processes observed *in situ* are much faster than those
12
13 occurring in cells because of the higher concentration of ROS (around 10^{-5} M^{24} *versus* less than
14
15 10^{-6} M in phagosome³⁶), the two mechanisms of degradation can also explain the thinner and
16
17 highly-perforated walls of the tubes extracted from macrophages. The non-site-specific thinning
18
19 certainly allows the exposition of sub-surface defects to ROS resulting in the drilling of many
20
21 holes in MWCNTs.
22
23
24
25
26

27 **Biological pathway for MWCNT degradation by macrophages.**

28
29
30
31 As both *in situ* and *in vitro* nanoscale studies suggest the crucial role of ROS in the degradation of
32
33 MWCNTs, we focused on the biological pathway for the production of ROS and particularly OH^{\bullet} .
34
35 In cells, MWCNTs are degraded into phagosomes,³ and NOX_2 complex is well known to be
36
37 associated with the plasma and the phagosomal membranes. This enzymatic complex was
38
39 described to be a biocatalyst of the reduction of molecular oxygen to generate superoxide $\text{O}_2^{\bullet-}$ that
40
41 can dismute to generate ROS species.³⁷ NOX -family enzymes are likely to be involved in a variety
42
43 of physiological events including cell proliferation, host defense, differentiation, apoptosis,
44
45 senescence and activation of growth-related signaling pathways.³⁷ NOX_2 complex consists of a
46
47 large association of glycoproteins named $\text{NOX}_{2\alpha}$ (or gp22phox), $\text{NOX}_{2\beta}$ (or gp91phox) and
48
49 cytosolic proteins, namely p67phox, p47phox, p40phox and Rac.³⁷ To assess the involvement of
50
51 NOX_2 complex into the degradation processes, macrophages were exposed for 24h to 5 $\mu\text{g/ml}$ of
52
53 MWCNTs or Fe@MWCNTs and total ribonucleic acid (RNA) were extracted. The mRNA of
54
55
56
57
58
59
60

1
2
3 NOX_{2α}, NOX_{2β}, p67phox, p47phox and p40phox were quantified by polymerase chain reaction
4
5 (PCR) (Figure 5a). The mRNAs of all of these proteins were approximatively induced two times
6
7 as compared to the untreated cells. The protein level for NOX_{2β} was also assessed by western blot
8
9 analysis. Both inductions at the genetic and protein levels are in good agreement (Figure S8).
10
11 Remarkably in the presence of NAC, no significant or much lower inductions were measured.
12
13 Together with the nanoscale investigations of the degraded MWCNTs, the biological response of
14
15 macrophages indicates a MWCNT-induced activation of NOX₂ complex and a subsequent
16
17 production of ROS with the purpose of degrading exogenous nanostructures. The addition of NAC
18
19 in the cellular medium inhibits the existing ROS and perturbs the retroactivity of ROS-production
20
21 by NOX₂, resulting in the low activity of this complex and the lower capacity of cells to degrade
22
23 MWCNTs.
24
25
26
27
28
29

30
31 When activated, NOX₂ complex is the most important source of ROS in phagocytes by O₂^{•-}
32
33 production³⁶. In the presence of superoxide dismutase (SOD), O₂^{•-} can dismutate into H₂O₂. As
34
35 described by Haber-Weiss reaction, in the presence of iron, O₂^{•-} and H₂O₂ produce OH[•]. We
36
37 evaluated this possible production pathway of OH[•] by quantifying SOD mRNA (Figure 5b). Cu-
38
39 SOD that is preferentially located into cytoplasm was induced 1.7 times as compared to control.
40
41 NAC did not change mRNA level of this protein. Mn-SOD that is preferentially located into
42
43 phagosome, was induced more than 2 times for MWCNTs and Fe@MWCNTs, but the presence
44
45 of NAC annihilates this enhanced-mRNA level. Note that mRNA of glutathione S-transferase
46
47 (GSTP-1), a well-known antioxidant, also increases most probably to regulate ROS production
48
49 (Figure 5b). Remarkably, Fe³⁺-catalyzed Haber-Weiss reaction³¹ and its metabolism seems to play
50
51 a role in the regulation of CNTs degradation *via* the production of iron storage proteins, such as
52
53 ferritin. Indeed both light chain (FerL) and heavy chain (FerH) of ferritin mRNA were induced by
54
55
56
57
58
59
60

1
2
3 MWCNT and Fe@MWCNT exposure (Figure 5c), as well as the protein level for FerH (figure
4 S8). Nevertheless, FerH mRNA was much less increased with Fe@MWCNTs than with
5
6
7
8 MWCNTs. This phenomenon indicates that the regulation of Fe^{3+} involved in the production of
9
10 OH^{\bullet} , is influenced by the presence of magnetite nanoparticles (composed of both Fe^{2+} and Fe^{3+}
11 ions) inside the nanotubes. With iron-free nanotubes, the cells need to provide more Fe^{3+} ions and
12 then produce more ferritin. With Fe@MWCNT, the cells reduce the endogenous production of
13 Fe^{3+} ions, because of the exogenous $\text{Fe}^{3+}/\text{Fe}^{2+}$ pool inside the tubes. These perturbations in the
14 iron-production mechanisms employed by macrophages to degrade carbon nanotubes could
15 generate different production rate of OH^{\bullet} and could then be responsible for the slightly different
16 degradation kinetics of MWCNTs and Fe@MWCNTs. For example, after 168h of incubation only
17 40.5% of total surface area for Fe@MWCNTs versus 51.1% for MWCNTs was degraded (Figure
18 1b).

19
20
21
22
23
24
25
26
27
28
29
30
31
32 As iNOS and MPO proteins were described to take part in CNT biodegradation,^{10, 16} their roles
33 were also investigated. Peroxynitrite-induced CNTs degradation was reported to play a significant,
34 but not exclusive, role in the biodegradation process,¹⁶ Peroxynitrite production in cells is due to
35 a non-enzymatic reaction of superoxide radicals and NO^{\bullet} .^{38, 39} In presence of MWCNT and
36 Fe@MWCNT, iNOS mRNA was quantified as NO^{\bullet} producer in cells. Interestingly, iNOS mRNA
37 was only increased in presence of Fe@MWCNT (Figure 5d) suggesting the ability of peroxynitrite
38 to preferentially attack structural defect site constituted by the presence of iron. As MPO was
39 described to take part in CNT degradation,¹¹ its mRNA expression was also quantified. Total
40 mRNA for MPO was increased by 38% in treated cells compared to the control (Figure 5d),
41 suggesting a possible implication of this protein in CNT degradation. Nevertheless, studies on
42
43
44
45
46
47
48
49
50
51
52
53
54
55
56
57
58
59
60

1
2
3 ROS produced by MPO in response to bacterial attack are mainly found in the extracellular
4 matrix³⁶ indicating that MPO could be produced by cells to induce extracellular CNT degradation.
5
6

7
8
9 As sketched in Figure 6, macrophages employed several oxidative mechanisms to degrade CNTs
10 outside and inside the cells. Particularly, our pluridisciplinary approach of MWCNT
11 biodegradation in macrophages sheds light on a multistep process based on the phagocytosis of
12 MWCNTs, the activation of NOX₂ complex into phagosomes with the purpose of producing ROS,
13 leading to the chemical attack of the graphitic nanostructures by OH[•]. Furthermore, the implication
14 of NOX₂ in the cell response to CNT allows highlighting many *in vitro* and *in vivo* studies on
15 CNTs. NOX₂ complex need to be associated with Rac₂ protein for its activation. Rho-GDP
16 dissociation inhibitor (Rho GDI) is a small protein associated to Rac₂-GDP in the cytoplasm.³⁷ To
17 be activated and move from the cytoplasm to the membrane, Rac₂ changes his GDP to GTP. This
18 modification leads to the dissociation of Rac₂ and Rho GDI explaining the induction of Rho GDI
19 protein alone in cells. Hence the activation of NOX₂ complex demonstrated in this study could
20 explain previous proteomic studies showing CNT- induced over-activity of Rho GDI.⁴⁰⁻⁴²
21
22 Moreover, it was also established that CNTs could cause cytoskeleton protein variations in
23 macrophages,^{41, 43} alveolar basal epithelial cells⁴⁰ or keratinocytes.⁴² Notably, Ju *et al.*
24 demonstrated that MWCNTs increase the actin expression in A549 cells, but this effect is
25 significantly attenuated by the inhibition of ROS by NAC.⁴⁰ These results are in line with the
26 NAC-induced low activity of NOX₂ complex, because p47phox has the ability to influence
27 cytoskeletal organization.⁴⁴ Our results are also supported by an *in vivo* study on knockout mice
28 that cannot produce NOX₂ β .⁴⁵ After a single instillation of 40 μ g of SWCNTs in the lung, alveolar
29 macrophages and neutrophils were found in larger numbers in the bronchoalveolar fluid of
30 knockout mice compared to normal mice. This cell accumulation was associated with production
31
32
33
34
35
36
37
38
39
40
41
42
43
44
45
46
47
48
49
50
51
52
53
54
55
56
57
58
59
60

1
2
3 of pro-inflammatory cytokines (IL6, MCP-1, TNF) and suppression of the anti-inflammatory/pro-
4
5 fibrotic response (TGF β) that are ordinarily induced by CNTs in mice that cannot clear them.⁴⁶⁻⁴⁸
6
7

8 In light of the present study, we could conclude that in the absence of NOX₂ β , CNTs could not be
9
10 degraded and pro-inflammatory response was activated. In another study, Shvedova *et al.* have
11
12 shown that vitamin E deficiency enhances pulmonary inflammatory response and oxidative stress
13
14 induced by SWCNTs in mice.⁴⁹ Interestingly, a study performed on HIV-gp120 protein revealed
15
16 the ability of vitamin E to regulate ROS generated by NOX₂ complex, supporting the role of NOX₂
17
18 complex in the degradation of CNTs and the role of pro-inflammatory cytokine as regulator of cell
19
20 response to CNTs.
21
22
23
24

25 26 **Conclusion**

27
28
29 The biodegradation of MWCNTs in macrophages was investigated by simultaneously examining
30
31 the influences of intracellular environment on the atomic structure of nanomaterials and probing
32
33 the genetic responses of the cells to CNTs. Liquid-cell TEM was exploited for the first time to
34
35 follow the dynamical chemical attack of MWCNTs by OH \cdot at the nanoscale, revealing two electron
36
37 dose-dependent routes of degradation: fast tearing and perforation of the walls are enabled on
38
39 reactive structural defects, while a continuous thinning of the walls occurs in a non-site-specific
40
41 manner. These nanoscale observations provide a mechanistic understanding of the ROS-induced
42
43 transformations of MWCNTs that could be exploited for drug delivery applications and for better
44
45 controlling the life-cycle of CNTs in biological environments. The crucial role of NOX₂ complex
46
47 in the biological pathway leading to a controlled production of ROS in the vicinity of MWCNTs
48
49 and their subsequent degradation was clearly established. These intracellular transformations,
50
51 together with the already revealed extra-cellular degradation of CNTs,¹⁶ emphasize on the various
52
53
54
55
56
57
58
59
60

1
2
3 oxidative mechanisms deployed by macrophages to process graphitic nanostructures. More
4
5 generally, this interdisciplinary approach to study the reciprocal interactions between endogenous
6
7 and exogenous species should be applied to others nanosystems and biological environments,
8
9 because it provides crucial information for the development of efficient and safe nanomedicine.
10
11
12
13
14
15
16
17
18
19

20 **Methods**

21
22
23 **Synthesis of MWCNTs and Fe@MWCNTs:** MWCNTs were provided by Pyrograph Products
24
25 (Cedarville, OH). Their inner diameter varies from 40 to 80 nm. As reported in previous study,¹⁷
26
27 to produce Fe@MWCNTs, MWCNTs were first washed with HNO₃ to remove traces of the
28
29 residual iron growth catalyst. To remove the maximum number of oxygenated species on their
30
31 surface they were heated at 900°C under an inert atmosphere for 4 h. The elimination of
32
33 oxygenated groups at the surface of MWCNTs was confirmed by X-ray photoelectron
34
35 spectroscopy.⁵⁰ MWCNTs were first dispersed in octadecene under ultrasonication. Iron stearate
36
37 was then added, and the solution was heated at 120°C for 12 h to dissolve the reactants, to eliminate
38
39 the traces of water or impurities, and to favor the diffusion of metal precursors inside MWCNTs.
40
41 Then, the mixtures were heated at 318°C (heating rate 5°C/min) under air for 2 h. Finally, the
42
43 products were washed four times with ethanol and chloroform, then centrifuged, followed by a
44
45 conventional filtration method to remove NPs formed outside MWCNTs.⁵¹ After this first filling
46
47 step, once the mixture was heated and cooled to room temperature, the same synthesis was repeated
48
49 again without washing steps by adding iron stearate as a precursor.
50
51
52
53
54
55
56
57
58
59
60

1
2
3 **Functionalization of MWCNTs and Fe@MWCNTs:** MWCNTs and Fe@MWCNTs were
4 functionalized by arylation to introduce amino groups on their sidewall and increase their
5 dispersibility in water.¹⁷ Iron Mass Fraction was quantified in previous study¹⁷ by ICP-AES
6 revealing the absence of iron for MWCNT and an iron mass fraction of 6.64% for Fe@MWCNT.
7
8
9

10
11 **Preparation and characterization of MWCNT and Fe@MWCNT suspensions:** Nanotubes
12 were suspended in cell culture media at a concentration of 100 µg/ml. The suspensions were
13 sonicated for 5 min (5s pause every 30s) at 60 W with an ultrasonic bath (sonorex digitec,
14 Bandelin). The quality of the suspensions was visually estimated and agglomerates sizes were
15 quantified using nanoparticle tracking analysis system (Nanosight, Malvern). Agglomerate mean
16 size was quantified to be 114±1.6 nm and 123.7±1.5 nm for MWCNT and Fe@MWCNT,
17 respectively. 90% of the agglomerates were smaller than 173±2.8 nm and 194.7±12.7 nm for
18 MWCNT and Fe@MWCNT, respectively.
19
20
21
22
23
24
25
26
27
28
29
30
31

32
33 **MWCNT for in vivo experiments:** MWCNT_{vi} (product number: 636649) was purchased from
34 Sigma -Aldrich (Lyon, France). These nanotubes were synthesized by Chemical Vapor Deposition
35 method. Their diameter ranged from 20 to 50 nm and their length from 0.5 to 2 µm (data from the
36 supplier).
37
38
39
40
41
42

43 **Cells and cytotoxicity test:** The human monocytic cell line THP-1 were obtained from ATCC
44 (France) and cultured in fresh supplemented media (RPMI 1640 medium supplemented with 10%
45 FCS (Gibco, France), 2 mM glutamine (Gibco, France), 100 U/ml penicillin, and 100 mg/ml
46 streptomycin (Gibco, France)) at 37 °C and 5% CO₂. The THP-1 cells were maintained between
47 10⁵ and 10⁶ cells/ml in fresh supplemented RPMI media. In the exponential phase of growth, cells
48 were seeded onto 96-well plates at 80,000 cells per well. After 48h phorbol myristate acetate
49
50
51
52
53
54
55
56
57
58
59
60

1
2
3 (PMA) treatment at 5 ng/ml, the cells were washed and exposed 24h to various concentrations of
4 MWCNTs or Fe@MWCNTs (0, 0.53, 1.06, 3.12, 6.25, 12.5, 25, 50, 75, 100 $\mu\text{g/ml}$) in RPMI
5
6
7
8 media. All the suspensions were prepared extemporary in tubes and 100 μl was added directly on
9
10 the cells. The cell viability was determined 24h after treatment by Alamar blue[®] assay (Alamar
11
12 blue[®] reagent, Biosource, France). At the end of the tests, optical density was measured on 80 μl
13
14 supernatant transferred in another clean culture plate.
15
16

17
18 **Oxidative stress assessment:** Cells were seeded onto 96-well plates at 80,000 cells per well in
19
20 presence of 5 ng/ml of PMA. After 48h, cells were washed and fresh supplemented media was
21
22 added for 24h. Then, cells were pre-treated or not for 30 min with 10 mM of NAC and exposed to
23
24 5 $\mu\text{g/ml}$ of MWCNTs or Fe@MWCNTs in the presence or absence of NAC. After 24h, cells were
25
26 washed with PBS, loaded with 50 μM of 2,7-dichlorofluorescein diacetate (DCF-DA) for 40 min
27
28 and washed again with PBS. After a further incubation in PBS for 1 h the fluorescence intensities
29
30 were measured at 488 nm excitation and 530 nm emission in the fluorescence plate reader (Fluostar
31
32 Galaxy CTC 435,BMG).
33
34
35

36
37
38 **Animals:** Male Sprague-Dawley rats weighing 180–220 g were purchased from Charles River
39
40 Laboratories (St Germain-sur-l'Arbresle, France). The rats were kept in a conventional animal
41
42 facility and had access ad libitum to food and drink. The experimental protocol has been approved
43
44 by the local ethical committee for animal research.
45
46
47

48
49 **TEM experiments:** All the *in situ* and *in vitro* TEM experiments were realized on the JEOL ARM
50
51 200F microscope equipped together with a CEOS aberration corrector for the objective lens and a
52
53 cold FEG. All the experiments were performed with an 80 kV acceleration voltage.⁵²
54
55
56
57
58
59
60

1
2
3
4
5
6
7
8
9
10
11
12
13
14
15
16
17
18
19
20
21
22
23
24
25
26
27
28
29
30
31
32
33
34
35
36
37
38
39
40
41
42
43
44
45
46
47
48

TEM structural analyses of MWCNTs and Fe@MWCNTs after aging in THP-1-derived macrophages : Cells were seeded onto 75 cm² flasks at 12.10⁶ cells per flask in presence of 5 ng/ml of PMA. After 48h, cells were washed and fresh supplemented media was added for 24 h. Then, cells were pre-treated or not for 30 min with 10 mM of NAC and exposed to 5 µg/ml of MWCNTs or Fe@MWCNTs in the presence or absence of NAC. After 24h incubation time, cells were washed with PBS and fresh supplemented media was added in order to remove the non-phagocytized nanomaterials. Three hours, 24h, 48h or 168h after exposure, cells were scraped and a centrifugation step at 350g for 10 min was performed to separate the cells from the media. Cells were suspended in presence of 200 µl of distilled water in a sonication bath at maximum power for 1 min, to lyse them by osmotic shock. Cell lysate was then centrifuged at 10,000g for 5 min. Supernatant was eliminated by pipetting and the pellet containing MWCNTs and cell residues was dispersed in water. After a final heating step at 80°C for 15 min to remove the last cell residues, 10 µl of the suspensions was deposited on carbon TEM grid and then dried for 5 min before TEM and HRTEM observations. To confirm that this extraction procedure did not affect the structure of the MWCNTs a control sample was realized on 3 ml of suspension used to expose the cells. To compare MWCNTs extracted from cells and MWCNTs from control both heating (37°C for 3h to 168h aging time; 80°C for 15 min) and centrifugation steps (350g for 5 min and 10,000g for 5 min) were performed on the suspension in absence of cells. TEM analysis of this control sample revealed that the structure of MWCNTs is not disturbed by the extraction procedure.

49
50
51
52
53
54
55
56
57
58
59
60

Liquid-cell sample preparation: The liquid cells commercialized by Protochips Inc. consist of two silicon wafers with dimensions of 2×2 mm and 4.5×6 mm, called the small and large E-chips, respectively (Figure S9). Each E-chip has one 550 µm × 50 µm window covered by a 30 nm thick silicon-nitrite amorphous film. A 2.5 µL drop of MWCNT or Fe@MWCNT suspension dispersed

1
2
3 in water or in ethanol, was deposited on the electron transparent membrane of the small E-chip.
4
5 The large E-chip was then placed over the small one with their windows in cross-configuration,
6
7 giving a square field of view of 50 μm edge length. Therefore, the drop of solution was squeezed
8
9 in between the two E-chips in a volume defined by the thickness of the gold spacers on the small
10
11 E-chip (150 nm in our case). The entire chamber was then closed by the lid of the holder tip
12
13 resulting in a vacuum sealed liquid-cell. As illustrated in Figure S9, the impermeability of the
14
15 liquid cell is ensured by two concentric O-rings. We did not use the holder in flow mode. The
16
17 thickness of the spacers corresponds to the smallest liquid thickness crossed by the electron beam
18
19 during the TEM experiment. Indeed due to the outward bowing of the SiN membranes under
20
21 vacuum, the smallest liquid thickness is found at the corners of the viewing window. All the images
22
23 were recorded close to the corners for improving signal to noise ratio.
24
25
26
27
28
29

30 *In situ STEM imaging:* STEM HAADF imaging was performed without changing probe size (5C)
31
32 and condenser aperture (70 μm) in order to maintain a constant beam current (i_e). The latter was
33
34 measured on the phosphorescent screen of the microscope prior to insert the sample to determine
35
36 the dose rate focalized on the liquid cell ($i_e = 3.74 \times 10^8$ electron/s or 59.8 pA). MWCNT
37
38 degradation was followed by continuously recording 512 \times 512 images with a pixel dwell time of
39
40 5 μs . In electron microscopy the dose rate (\dot{d}) is usually calculated in electrons/ $\text{\AA}^2\text{s}$ by dividing i_e
41
42 by the surface irradiated by the beam, which in STEM mode advantageously corresponds to the
43
44 imaged area. Therefore, \dot{d} was easily controlled since it is inversely proportional to the square of
45
46 the magnification. With such optical conditions, \dot{d} varies from 4.5 to 32 electrons/ $\text{\AA}^2\text{s}$, with the
47
48 magnification used for imaging (from 150k to 400k). The conversion of \dot{d} in $\text{Gy}\cdot\text{s}^{-1}$ (*i.e.* $\text{J}\cdot\text{kg}^{-1}\cdot\text{s}^{-1}$),
49
50 units commonly used in the field of radiation chemistry, simply requires multiplying \dot{d} in
51
52 electron/ $\text{m}^2\cdot\text{s}$ by the density normalized stopping power of the solvent (4.761×10^5 and 4.961×10^5
53
54
55
56
57
58
59
60

1
2
3 eV·m²/kg per electron, at 80 kV for water and ethanol, respectively) and by 1.6 10⁻¹⁹ to convert
4
5 electron-volts to joules. This leads to \dot{d} in between 3.4×10⁷ and 2.4 10⁸ Gy·s⁻¹ for magnification
6
7 ranging from 150k to 400k in water. \dot{d} is slightly more important in ethanol for equivalent optical
8
9 conditions.
10

11
12
13 **Cytotoxicity of degradation products:** 24h after exposure, MWCNTs or Fe@MWCNTs were
14
15 extracted from cells (see extraction procedure above), the degraded MWCNTs and Fe@MWCNTs
16
17 were suspended in 100 μf of distilled water. The concentrations of the dMWCNT and
18
19 dFe@MWCNT suspensions were then quantified using DO₂₇₃ quantification method⁵³ against a
20
21 standard range of MWCNTs or Fe@MWCNTs. Cytotoxicity tests were then performed by Alamar
22
23 blue assay for different concentration of dMWCNT and dFe@MWCNT following the same
24
25 procedure than for MWCNTs and Fe@MWCNTs (see procedure above)
26
27
28
29
30

31 **In vivo degradation of MWCNT assessment:** 3 rats were exposed to 100 μg of MWCNT by
32
33 intratracheal instillation. 7 days after the exposure, the animals were anesthetized. The lungs and
34
35 the lymph nodes were removed, cut in small sections and fixed with 2.5% glutaraldehyde. After a
36
37 postfixation with 1% osmium tetroxide, the samples were dehydrated by ethanol and embedded in
38
39 EPON 812 (TAAB). The ultrathin sections of 90 nm and 150 nm respectively for TEM analyses
40
41 were obtained by an ultramicrotome (UCT, Leica), mounted on copper grids and stained with
42
43 uranyl acetate and examined in a Tecnai G₂ Biotwin (FEI) electron microscope using an
44
45 accelerating voltage of 100 kV. Several photographs of MWCNT_{vi} detailed structures were taken
46
47 analyzed and compared to control samples.
48
49
50
51
52

53 **NOX₂ complex and antioxidant protein markers by reverse transcription real time**
54
55 **polymerase chain reaction (RT-qPCR):** Cells were seeded onto 6-well plates at 2×10⁶ cells per
56
57
58
59
60

1
2
3 well in presence of 5 ng/ml of PMA. After 48h, cells were washed and fresh supplemented media
4
5 was added for 24h. Then, cells were pre-treated or not for 30 min with 10 mM of NAC and exposed
6
7 to 5 µg/ml of MWCNTs or Fe@MWCNTs in presence or absence of NAC. After 24h, cells were
8
9 washed with PBS and total RNA was extracted from 10⁶ cells with NucleoSpin RNA II[®] Kit
10
11 (Macherey Nagel) according to manufacturer's protocol. One µg of total RNA was reverse
12
13 transcribed to cDNA with SuperScript[®] Reverse Transcriptase (Invitrogen, Cat n°18064-014)
14
15 according to the manufacture's protocol using Random primer (Promega, Cat n°C1181) and
16
17 RNasin (Promega, Cat n°N2511). The quantification of mRNA for RPL19 (housekeeping gene,
18
19 Fwd 5'-TCATCAAAGATGGGCTGATCAT-3'; Rev 5'-CATCGAGCCCGGAATG-3');
20
21 NOX_{2α} (Fwd 5'-GGGCCCTTTACCAGGAATTACT-3'; Rev 5'-
22
23 GGCACCGAGAGCAGGAGAT-3'); NOX_{2β} (Fwd 5'-TGTGTGAATGCCCGAGTCAA-3'; Rev
24
25 5'-TACAGGCCTCCTTCAGGGTT-3'); p47phox (Fwd 5'-CCCATCATCCTGCAGACGTA-3';
26
27 Rev 5'-GAGCCCGAGGTCTTCTCGTA-3'); p40phox (Fwd 5'-
28
29 AGCTCACAAGGCGGGAGTT-3'; Rev 5'-TCAGCGTCCCGGTAATTCAG-3'); p67phox
30
31 (Fwd 5'-GCCCAGACATTCCAAAATCG-3'; Rev 5'-GGCTCATATAGCTTCTGCTTCCA-
32
33 3'); MPO (Fwd 5'-GCCAAGCTGAATCGTCAGAAC-3'; Rev 5'-
34
35 TCATGACCTGCTCAAACAATCG-3'); SOD-Cu (Fwd 5'-CAGGGCATCATCAATTTTCA-
36
37 3'; Rev 5'-TGCTTCCCCACACCTTCAC-3'); SOD-Mn (Fwd 5'-CGCGGCCTACGTGAACA-
38
39 3'; Rev 5'-CCAACGCCTCCTGGTACTTC-3'); GSTP1 (Fwd 5'-
40
41 CGGGCAACTGAAGCCTTTT-3'; Rev 5'-AAGGTCTTGCCTCCCTGGTT-3'); Ferritin L (Fwd
42
43 5'-CGAATTGGCCGAGGAGAA-3'; Rev 5'-GCCACGCTGGTTTTGCAT-3'); Ferritin H (Fwd
44
45 5'-TGGCTTGGCGGAATTTCTGT-3'; Rev 5'-GCCCCGAGGCTTAGCTTTCAT-3'); iNOS
46
47 (Fwd 5'-CCCCTTCAATGGCTGGTACA-3'; Rev 5'-GCGCTGGACGTCACAGAA-3')

1
2
3 transcript were performed using SYBR® green PCR master Mix (Applied Biosystems, Cat
4 n°4367659) according to the manufacturer's protocol on 300 ng of cDNA using StepOne plus
5
6
7
8 Mastercycler (Applied Biosystems). Each sample was run in duplicate.
9

10
11 **Protein quantification performed by western blot analysis:** Cells were seeded onto 6-well
12 plates at 2×10^6 cells per well in presence of 5 ng/ml of PMA. After 48h, cells were washed and
13 fresh supplemented media was added for 24h. Then, cells were pre-treated or not for 30 min with
14
15
16
17 10 mM of NAC and exposed to 5 $\mu\text{g/ml}$ of MWCNTs or Fe@MWCNTs in presence or absence
18
19 of NAC. After 24h, cells were washed with PBS and proteins were extracted with Nucler/Cytosol
20
21
22
23 fractionation Kit (Biovision) according to manufacturer's protocol. Presence of NOX_{2 β} and
24
25
26
27 Ferritin H were analyzed on 50 μg of cytosolic protein by SDS-PAGE (4-20% polyacrylamide,
28
29 Mniprotean TGX, Biorad). Separated proteins were transferred onto nitrocellulose membranes.
30
31
32
33 Blots were saturated 1h in TBST (Tris-base, pH 7.4, Tween 20 %)-5% BSA and washed in TBST
34
35
36
37 (3x5 min). They were subsequently incubated for 2 h with a rabbit NOX_{2 β} or Ferritin H antibody
38
39
40
41 (Santa Cruz) diluted at 1:300 in TBST-BSA 3%. After washing in TBST (3x5 min), the membranes
42
43
44
45 were reacted with a goat anti-rabbit-HRP antibody (Santa Cruz) diluted at 1:3300 in TBST-BSA
46
47
48
49
50
51
52
53
54
55
56
57
58
59
60
To compare the effect of each treatment, a R_d ratio was calculated as follow:

$$R_d = \frac{D_{ex1} \times D_{con2}}{D_{ex2} \times D_{con1}}$$

Where D_{ex1} , D_{ex2} are the densities of exposed groups for NOX_{2 β} (or FerH) and RPL19 and D_{con1}
and D_{con2} are the densities of control groups for NOX_{2 β} (or FerH) and RPL19.

1
2
3 **Statistics:** All data were expressed as mean \pm S.D (standard deviation). F-test was used to compare
4 the homogeneity of the variances. If homogeneity of variance was verified with a risk alpha equal
5 to 5 %, differences between each group were assessed with a one-way analysis of variance
6 (ANOVA). When all ANOVA tests were positive, groups were subjected to the multiple-
7 comparison Dunnett's test. If the variances were not homogeneous, no significant differences
8 between groups were considered. *P < 0.05 was considered as the statistical significance level.
9 For each aging time point 3h, 24h, 48h, 168h of CNTs in cells in presence or absence of NAC,
10 percentage of perforated area (P_a), the mean surface area of holes (\bar{S}) and the density of holes (D)
11 were measured in MWCNTs and Fe@MWCNTs. Hole surface areas at each time point could be
12 assimilated as a distribution and then compared per pair using Kolmogorov Smirnov test. P-values
13 obtained by Kolmogorov-Smirnov test which are less than 0.05 show significant differences
14 between the two distributions.
15
16
17
18
19
20
21
22
23
24
25
26
27
28
29
30
31
32
33
34
35
36
37
38
39
40
41
42
43
44
45
46
47
48
49
50
51
52
53
54
55
56
57
58
59
60

FIGURES

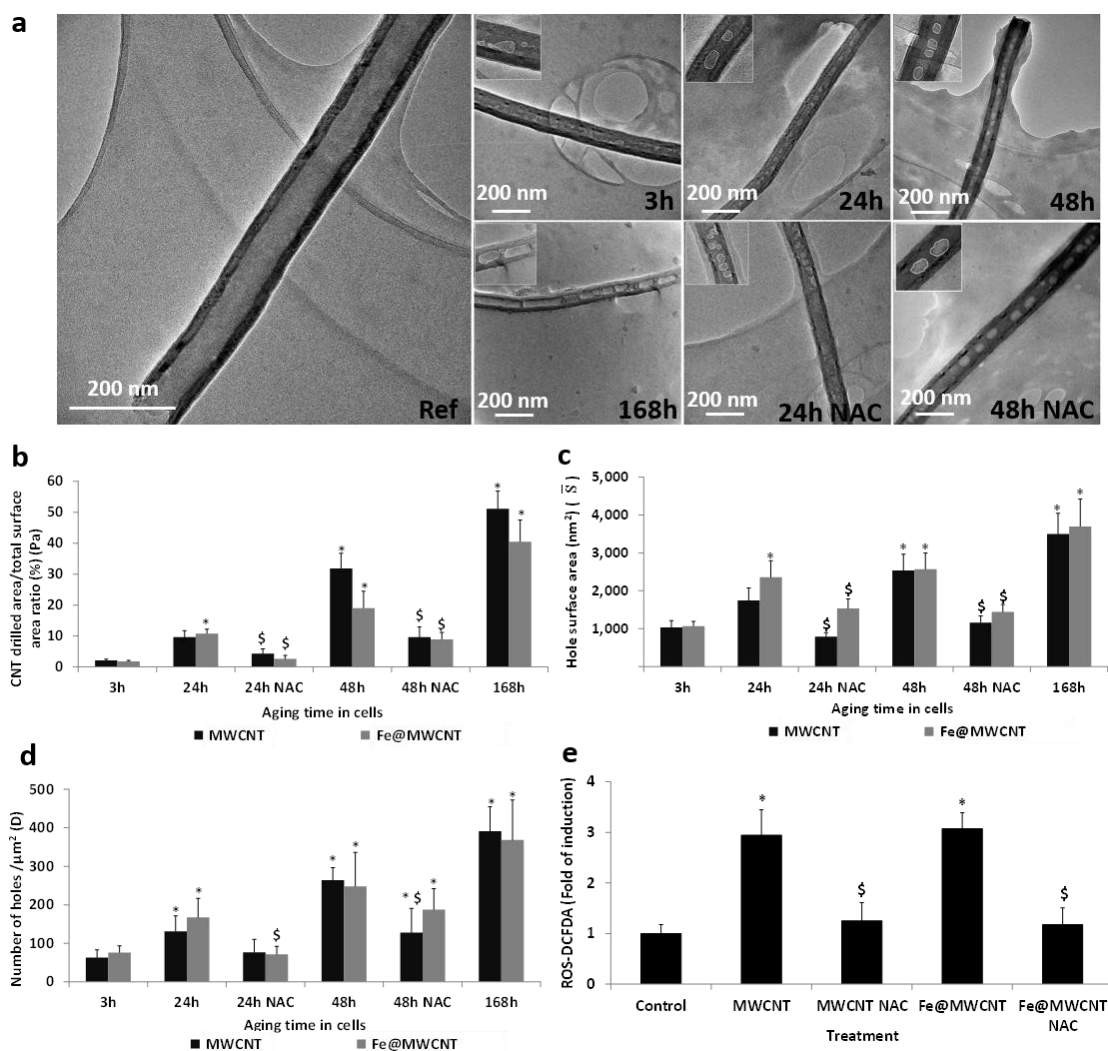


Figure 1. MWCNT and Fe@MWCNT degradation in THP-1 differentiated into macrophages. a, TEM observations of MWCNTs before (Ref) and after aging into cells. The aging time and the presence of NAC in cells are indicated in the bottom right corner of each image. b, Ratio of total perforated area to total surface area (P_a), c, mean surface area of holes (\bar{S}) and d, density of holes (D) in MWCNTs or Fe@MWCNTs as a function of the aging time in cells and the presence or absence of NAC. e, Formation of ROS in THP-1 after treatment with a 5 $\mu\text{g}/\text{ml}$ suspension of MWCNTs or Fe@MWCNTs for 24 h. ROS were detected by fluorescence measurement of the DCFDA reporter and results are given in fold of untreated controls. Data shown in panels b, c and d are from three independent experiments (minimum 50 observed items) and are expressed as mean values \pm S.D. Results in panel e are the mean \pm SD of 3 separate experiments, each carried in triplicates. (*) Designates a statistically-significant difference from 3h group ($p < 0.05$) (panel b, c and d) or control group (panel e). (\$) Designates a statistically-significant difference between MWCNT NAC or Fe@MWCNT NAC groups and its respective equivalent MWCNT or Fe@MWCNT group without NAC treatment ($p < 0.05$).

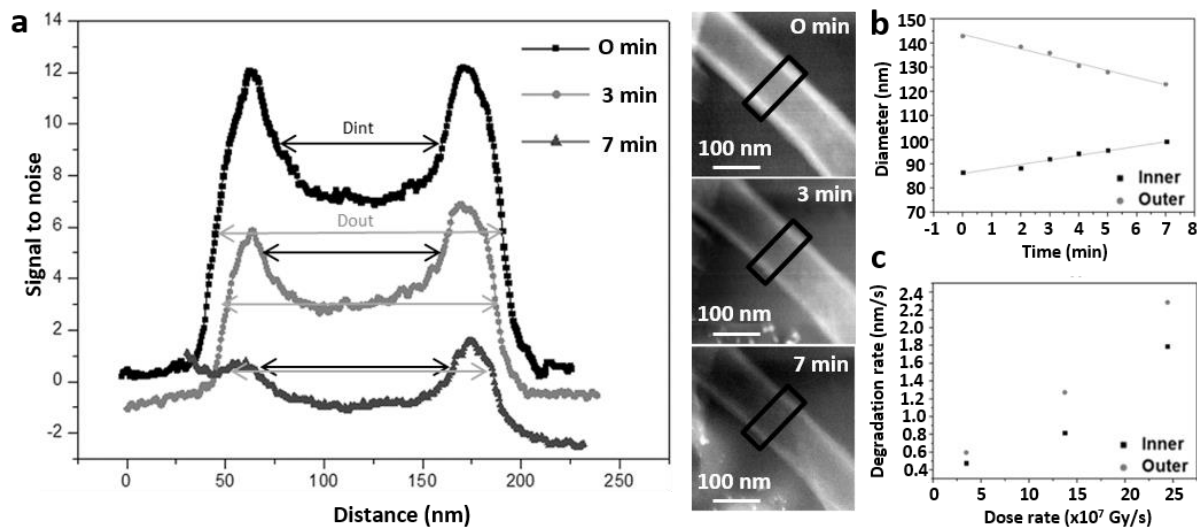


Figure 2. *In situ* liquid TEM in water. Dose-dependent thinning of MWCNTs due to $\text{OH}\cdot$ produced by radiolysis. a, Time evolution of signal-to-noise ratio (SNR) profile measured across a MWCNT, during non-site-specific degradation. The position and the width (100 nm) of the SNR profiles are indicated on the three STEM-HAADF images acquired at 400k magnification (corresponding dose rate of 2.4×10^8 Gy.s $^{-1}$, see method section) after 0, 3 and 7 min of irradiation. The inner (D_{int}) and outer (D_{out}) diameters were measured by considering the position of the sidewalls as the half maximum of the corresponding peaks on the SNR profiles. b, Time evolution of the inner and outer diameters of the MWCNT degraded in (a). The concomitant increase of the inner diameter and decrease of the outer diameter reveal that degradation occurs inside and outside of the MWCNTs. Linear regressions were applied to the size evolution of inner and outer diameters as a function of time, from which the slope corresponds to their kinetic of degradation. c, Degradation rate (nm/s) of the inner and outer diameters of CNT as a function of the electron dose given in Gy.s $^{-1}$ (see Methods).

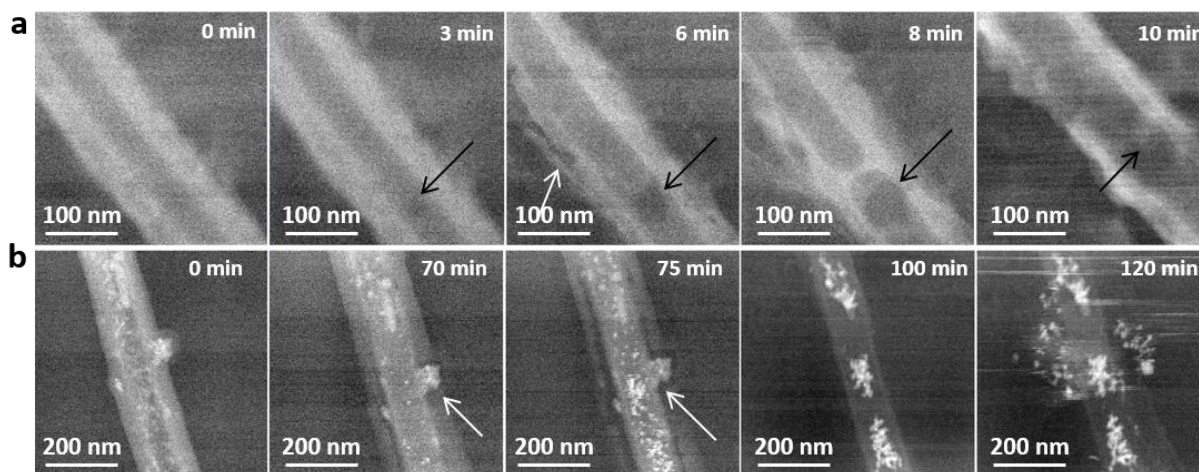


Figure 3. *In situ* liquid TEM in water. Site-specific drilling of MWCNTs induced by OH• chemical attack. Time series of STEM-HAADF images with the observation time indicated in the top right corner of each image. a, Drilling process in a MWCNT acquired with a magnification of 400k (corresponding dose rate of 2.4×10^8 Gy.s⁻¹, see method section). Black arrows indicate the nucleation and growth of a spherical hole and the white arrow shows a tearing of the nanotube along the anisotropy axis. A video file of this image series accelerated 16 times can be seen in supplementary. b Drilling process in a Fe@MWCNT acquired with a magnification of 200k (corresponding dose rate of 6×10^7 Gy.s⁻¹, see Method). White arrows show a tearing of the nanotube along the interface between the graphitic structure and the iron oxide nanoparticles inserted in the carbon walls.

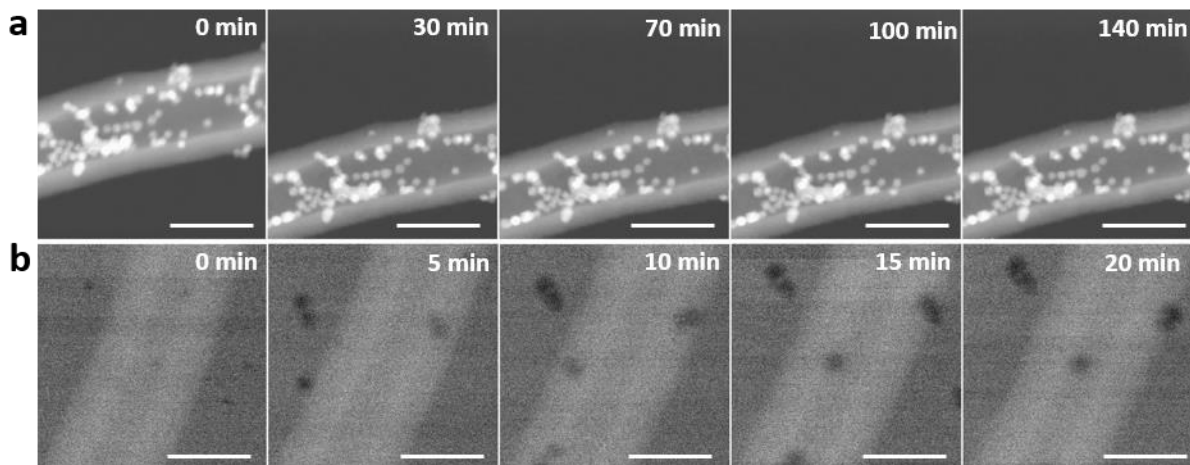


Figure 4: Stability of MWCNTs and Fe@MWCNTs under similar beam irradiation conditions in vacuum and in ethanol. STEM HAADF image series acquired at 80 kV with a magnification of 400k. The observation time on the analyzed area is indicated in the top right corner of each image. **a**, No degradation of Fe@MWCNTs is observed under vacuum condition (conventional STEM observation) revealing the absence of knock-on damage induced by electron beam. **b**, No degradation of MWCNTs is observed in ethanol in which the electron beam creates peroxy groups but no OH^{*} (circular black contrasts are imaging artefacts). Scale bars correspond to 100 nm in each image

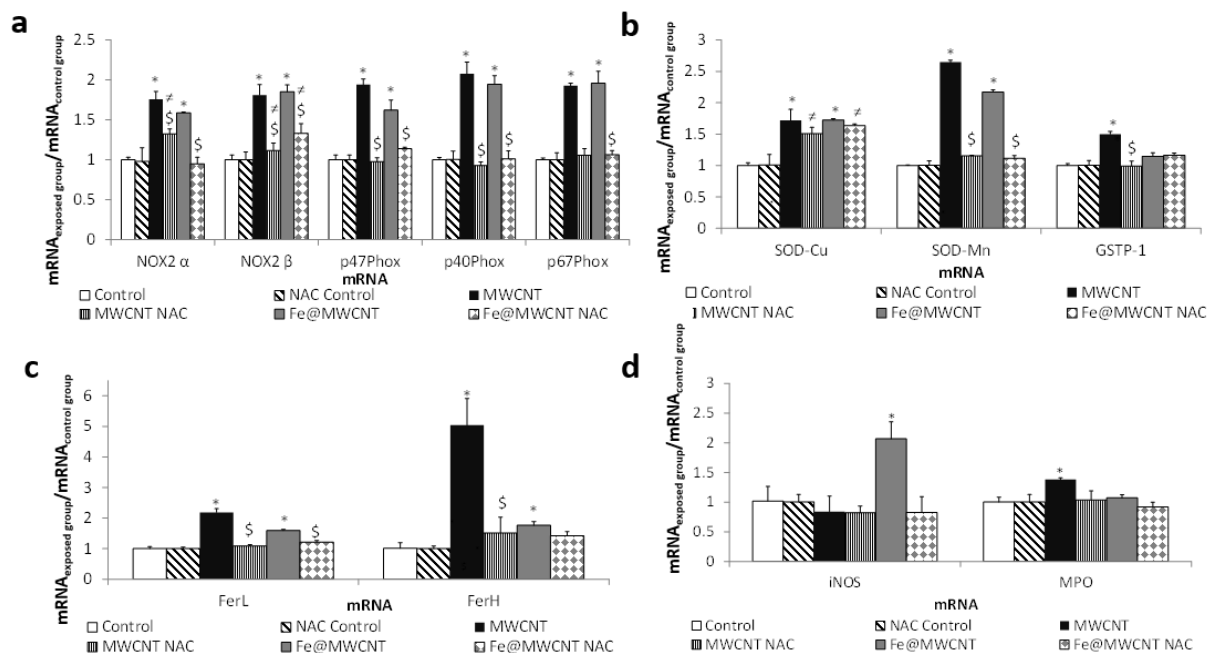


Figure 5. Effect of MWCNTs and Fe@MWCNTs on the gene expression level of NOX₂ complex and antioxidant proteins. THP-1 cells were treated with 5 $\mu\text{g}/\text{ml}$ of MWCNT or Fe@MWCNT suspension. After 24h exposure, mRNA quantification of a, NOX2 α , NOX2 β , p47phox, p40phox, and p67phox; b, SOD-Cu, SOD-Mn and GSTP1; c, Ferritin L and Ferritin H; and d, INOS and MPO. Results are the mean \pm SD of 3 separate experiments. (*) Designates a statistically-significant difference from control group ($p < 0.05$). (\$) Designates a statistically-significant difference between MWCNTs NAC or Fe@MWCNT NAC group and its respectively equivalent MWCNTs or Fe@MWCNTs group without NAC treatment ($p < 0.05$). (#) Designates a statistically-significant difference between MWCNT NAC or Fe@MWCNTs NAC and NAC control group ($p < 0.05$).

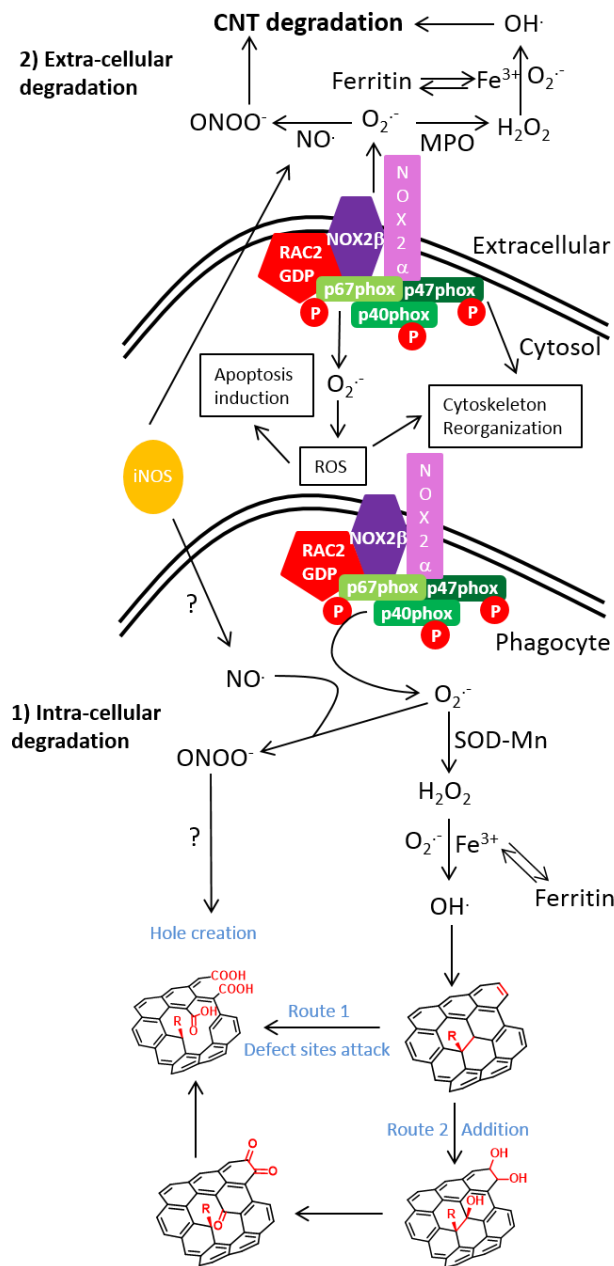


Figure 6. Schematic representation of the biological pathways of MWCNT degradation in macrophages. 1) Intracellular oxidative degradation: After engulfment of MWCNTs, NOX₂ complex is activated on cytosolic and phagosomal membranes. Active NOX₂ complex induced O₂^{•-} production and then cytoskeleton reorganization. Into phagosome, O₂^{•-} is turned into H₂O₂ by SOD and H₂O₂ is turned in presence of Fe³⁺ into OH[•] (Haber-Weiss reaction). OH[•] could attack MWCNT defects and unsaturated carbon bonds on the sidewalls of CNTs to generate carboxylic acids creating holes in the graphitic structure. 2) Extracellular oxidative degradation: MWCNT outside the cells can also be degraded by two routes: (i) Production of OH[•] via NOX₂ complex and MPO, or (ii) Peroxynitrique attack as described by kagan et al.¹⁶

1
2
3
4
5 ASSOCIATED CONTENT
6
7

8
9 **Supporting Information.** Supplementary figures and a video accelerated 16 times of nanotube
10 degradation in water (corresponding to figure 3a) are available free of charge *via* the Internet at
11 <http://pubs.acs.org>.”
12
13
14
15

16
17
18
19 AUTHOR INFORMATION
20
21

22 **Corresponding Author**
23

24
25 * Damien Alloyeau: alloyeau.damien@gmail.com and Florence Gazeau : [florence.gazeau@univ-](mailto:florence.gazeau@univ-paris-diderot.fr)
26 [paris-diderot.fr](mailto:florence.gazeau@univ-paris-diderot.fr)
27
28
29

30
31 **Author Contributions**
32

33 ‡These authors contributed equally.
34
35
36
37
38

39 ACKNOWLEDGMENT
40

41 This work was supported by the CNRS (Centre National de la Recherche Scientifique, Defi
42 Nano program), the ANR (Agence Nationale de la Recherche) and CGI (Commissariat à
43 l'Investissement d'Avenir) through the LabEx SEAM (Science and Engineering for Advanced
44 Materials and devices; ANR 11 LABX 086, ANR 11 IDEX 05 02) and the LabEx Chemistry of
45 Complex Systems (ANR-10-LABX-0026_CSC), by the ANR project DECANO (ANR-2011-
46 CESA-007-01) and by the International Center for Frontier Research in Chemistry (icFRC).
47
48
49
50
51
52
53
54
55
56
57
58
59
60

REFERENCES

1. Lanone, S.; Boczkowski, J. Biomedical Applications and Potential Health Risks of Nanomaterials: Molecular Mechanisms. *Curr Mol Med* **2006**, *6*, 651-63.
2. Sechi, G.; Bedognetti, D.; Sgarrella, F.; Van Eperen, L.; Marincola, F. M.; Bianco, A.; Delogu, L. G. The Perception of Nanotechnology and Nanomedicine: A Worldwide Social Media Study. *Nanomedicine* **2014**, *9*, 1475-86.
3. Elgrabli, D.; Floriani, M.; Abella-Gallart, S.; Meunier, L.; Gamez, C.; Delalain, P.; Rogerieux, F.; Boczkowski, J.; Lacroix, G. Biodistribution and Clearance of Instilled Carbon Nanotubes in Rat Lung. *Part Fibre Toxicol.* **2008**, *5*, 20.
4. McDevitt, M. R.; Chattopadhyay, D.; Kappel, B. J.; Jaggi, J. S.; Schiffman, S. R.; Antczak, C.; Njardarson, J. T.; Brentjens, R.; Scheinberg, D. A. Tumor Targeting with Antibody-Functionalized, Radiolabeled Carbon Nanotubes. *J Nucl Med* **2007**, *48*, 1180-1189.
5. Wang, H.; Wang, J.; Deng, X.; Sun, H.; Shi, Z.; Gu, Z.; Liu, Y.; Zhao, Y. Biodistribution of Carbon Single-Wall Carbon Nanotubes in Mice. *J Nanosci Nanotechnol* **2004**, *4*, 1019-24.
6. Shvedova, A. A.; Kisin, E. R.; Mercer, R.; Murray, A. R.; Johnson, V. J.; Potapovich, A. I.; Tyurina, Y. Y.; Gorelik, O.; Arepalli, S.; Schwegler-Berry, D., *et al.* Unusual Inflammatory and Fibrogenic Pulmonary Responses to Single-Walled Carbon Nanotubes in Mice. *Am J Physiol Lung Cell Mol Physiol* **2005**, *289*, L698-708.
7. Flaviu, T.; Catoi, C.; Mocan, T.; Mocan, L.; Biris, A.; Simon, S.; Nagy, A.; Taulescu, M.; BolfĂ, P.; Catoi, A. F. Interaction between Kupffer Cells and Carbon Nanotubes-Transition from Biodistribution and Toxicity to Kupffer Cell Targeted Therapy. *Bulletin of the University of Agricultural Sciences & Veterinary Medicine Cluj-Napoca. Veterinary Medicine* **2013**, *70*, 147.
8. Lacerda, L.; Ali-Boucetta, H.; Herrero, M. A.; Pastorin, G.; Bianco, A.; Prato, M.; Kostarelos, K. Tissue Histology and Physiology Following Intravenous Administration of Different Types of Functionalized Multiwalled Carbon Nanotubes. *Nanomedicine* **2008**, *3*, 149-61.
9. Cherukuri, P.; Bachilo, S. M.; Litovsky, S. H.; Weisman, R. B. Near-Infrared Fluorescence Microscopy of Single-Walled Carbon Nanotubes in Phagocytic Cells. *J. Am. Chem. Soc.* **2004**, *126*, 15638-15639.
10. Allen, B. L.; Kichambare, P. D.; Gou, P.; Vlasova, II; Kapralov, A. A.; Konduru, N.; Kagan, V. E.; Star, A. Biodegradation of Single-Walled Carbon Nanotubes through Enzymatic Catalysis. *Nano Lett* **2008**, *8*, 3899-903.
11. Kagan, V. E.; Konduru, N. V.; Feng, W.; Allen, B. L.; Conroy, J.; Volkov, Y.; Vlasova, II; Belikova, N. A.; Yanamala, N.; Kapralov, A., *et al.* Carbon Nanotubes Degraded by Neutrophil Myeloperoxidase Induce Less Pulmonary Inflammation. *Nat Nanotechnol* **2010**, *5*, 354-9.
12. Andon, F. T.; Kapralov, A. A.; Yanamala, N.; Feng, W.; Baygan, A.; Chambers, B. J.; Hultenby, K.; Ye, F.; Toprak, M. S.; Brandner, B. D., *et al.* Biodegradation of Single-Walled Carbon Nanotubes by Eosinophil Peroxidase. *Small* **2013**, *9*, 2721-2729.
13. Bhattacharya, K.; El-Sayed, R.; Andón, F. T.; Mukherjee, S. P.; Gregory, J.; Li, H.; Zhao, Y.; Seo, W.; Fornara, A.; Brandner, B., *et al.* Lactoperoxidase-Mediated Degradation of Single-Walled Carbon Nanotubes in the Presence of Pulmonary Surfactant. *Carbon* **2015**, *91*, 506-517.

- 1
2
3
4
5
6
7
8
9
10
11
12
13
14
15
16
17
18
19
20
21
22
23
24
25
26
27
28
29
30
31
32
33
34
35
36
37
38
39
40
41
42
43
44
45
46
47
48
49
50
51
52
53
54
55
56
57
58
59
60
14. Farrera, C.; Bhattacharya, K.; Lazzaretto, B.; Andon, F. T.; Hultenby, K.; Kotchey, G. P.; Star, A.; Fadeel, B. Extracellular Entrapment and Degradation of Single-Walled Carbon Nanotubes. *Nanoscale* **2014**, *6*, 6974-83.
 15. Russier, J.; Ménard-Moyon, C.; Venturelli, E.; Gravel, E.; Marcolongo, G.; Meneghetti, M.; Doris, E.; Bianco, A. Oxidative Biodegradation of Single- and Multi-Walled Carbon Nanotubes. *Nanoscale* **2011**, *3*, 893-6.
 16. Kagan, V. E.; Kapralov, A. A.; St Croix, C. M.; Watkins, S. C.; Kisin, E. R.; Kotchey, G. P.; Balasubramanian, K.; Vlasova, II; Yu, J.; Kim, K., *et al.* Lung Macrophages "Digest" Carbon Nanotubes Using a Superoxide/Peroxynitrite Oxidative Pathway. *ACS Nano* **2014**, *8*, 5610-21.
 17. Liu, X.; Marangon, I.; Melinte, G.; Wilhelm, C.; Ménard-Moyon, C.; Pichon, B. P.; Ersen, O.; Aubertin, K.; Baaziz, W.; Pham-Huu, C., *et al.* Design of Covalently Functionalized Carbon Nanotubes Filled with Metal Oxide Nanoparticles for Imaging, Therapy, and Magnetic Manipulation. *ACS Nano* **2014**, *8*, 11290-304.
 18. Kagan, V. E.; Tyurina, Y. Y.; Tyurin, V. A.; Konduru, N. V.; Potapovich, A. I.; Osipov, A. N.; Kisin, E. R.; Schwegler-Berry, D.; Mercer, R.; Castranova, V., *et al.* Direct and Indirect Effects of Single Walled Carbon Nanotubes on Raw 264.7 Macrophages: Role of Iron. *Toxicol Lett* **2006**, *165*, 88-100.
 19. Panasenkov, O. M.; Chekanov, A. V.; Arnhold, J.; Sergienko, V. I.; Osipov, A. N.; Vladimirov, Y. A. Generation of Free Radicals During Decomposition of Hydroperoxide in the Presence of Myeloperoxidase or Activated Neutrophils. *Biochemistry (Mosc)* **2005**, *70*, 998-1004.
 20. Zhao, Y.; Allen, B. L.; Star, A. Enzymatic Degradation of Multiwalled Carbon Nanotubes. *J Phys Chem A* **2011**, *115*, 9536-44.
 21. de Jonge, N.; Ross, F. M. Electron Microscopy of Specimens in Liquid. *Nat Nanotechnol* **2011**, *6*, 695-704.
 22. Williamson, M. J.; Tromp, R. M.; Vereecken, P. M.; Hull, R.; Ross, F. M. Dynamic Microscopy of Nanoscale Cluster Growth at the Solid-Liquid Interface. *Nat Mater* **2003**, *2*, 532-6.
 23. Woehl, T. J.; Jungjohann, K. L.; Evans, J. E.; Arslan, I.; Ristenpart, W. D.; Browning, N. D. Experimental Procedures to Mitigate Electron Beam Induced Artifacts During in Situ Fluid Imaging of Nanomaterials. *Ultramicroscopy* **2013**, *127*, 53-63.
 24. Schneider, N. M.; Norton, M. M.; Mendel, B. J.; Grogan, J. M.; Ross, F. M.; Bau, H. H. Electron-Water Interactions and Implications for Liquid Cell Electron Microscopy. *The Journal of Physical Chemistry C* **2014**, *118*, 22373-22382.
 25. De Clercq, A.; Dachraoui, W.; Margeat, O.; Pelzer, K.; Henry, C. R.; Giorgio, S. Growth of Pt-Pd Nanoparticles Studied in Situ by Hrtem in a Liquid Cell. *The Journal of Physical Chemistry Letters* **2014**, *5*, 2126-2130.
 26. Evans, J. E.; Jungjohann, K. L.; Browning, N. D.; Arslan, I. Controlled Growth of Nanoparticles from Solution with in Situ Liquid Transmission Electron Microscopy. *Nano Lett* **2011**, *11*, 2809-13.
 27. Zheng, H.; Smith, R. K.; Jun, Y. W.; Kisielowski, C.; Dahmen, U.; Alivisatos, A. P. Observation of Single Colloidal Platinum Nanocrystal Growth Trajectories. *Science* **2009**, *324*, 1309-12.
 28. Alloeyau, D.; Dachraoui, W.; Javed, Y.; Belkahla, H.; Wang, G.; Lecoq, H.; Ammar, S.; Ersen, O.; Wisnet, A.; Gazeau, F., *et al.* Unravelling Kinetic and Thermodynamic Effects on the

- 1
2
3 Growth of Gold Nanoplates by Liquid Transmission Electron Microscopy. *Nano Lett* **2015**, *15*,
4 2574–2581.
- 5
6 29. Liao, H. G.; Niu, K.; Zheng, H. Observation of Growth of Metal Nanoparticles. *Chem*
7 *Commun (Camb)* **2013**, *49*, 11720-7.
- 8
9 30. Zhao, Y.; Burkert, S. C.; Tang, Y.; Sorescu, D. C.; Kapralov, A. A.; Shurin, G. V.;
10 Shurin, M. R.; Kagan, V. E.; Star, A. Nano-Gold Corking and Enzymatic Uncorking of Carbon
11 Nanotube Cups. *J Am Chem Soc* **2015**, *137*, 675-84.
- 12
13 31. Gardes-Albert, M.; Bonnefont-Rousselot, D.; Abedinzadeh, Z.; Jore, D. Reactive Oxygen
14 Species. How Oxygen May Become Toxic? *L'Actualité chimique* **2003**, *11*, 91-96.
- 15
16 32. Li, W.; Bai, Y.; Zhang, Y.; Sun, M.; Cheng, R.; Xu, X.; Chen, Y.; Mo, Y. Effect of
17 Hydroxyl Radical on the Structure of Multi-Walled Carbon Nanotubes. *Synthetic Metals* **2005**,
18 *155*, 509-515.
- 19
20 33. Amiri, A.; Memarpoor-Yazdi, M.; Shanbedi, M.; Eshghi, H. Influence of Different
21 Amino Acid Groups on the Free Radical Scavenging Capability of Multi Walled Carbon
22 Nanotubes. *Journal of Biomedical Materials Research Part A* **2013**, *101A*, 2219-2228.
- 23
24 34. Shieh, Y.-T.; Wang, W.-W. Radical Scavenging Efficiencies of Modified and
25 Microwave-Treated Multiwalled Carbon Nanotubes. *Carbon* **2014**, *79*, 354-362.
- 26
27 35. Shukla, P. K.; Mishra, P. C. Effects of Diameter, Length, Chirality and Defects on the
28 Scavenging Action of Single-Walled Carbon Nanotubes for Oh Radicals: A Quantum
29 Computational Study. *Chemical Physics* **2010**, *369*, 101-107.
- 30
31 36. Dupre-Crochet, S.; Erard, M.; Nubetae, O. Ros Production in Phagocytes: Why, When,
32 and Where? *J Leukoc Biol* **2013**, *94*, 657-70.
- 33
34 37. Guichard, C.; Pedruzzi, E.; Fay, M.; Ben Mkaddem, S.; Coant, N.; Daniel, F.; Ogier-
35 Denis, E. The Nox/Duox Family of Ros-Generating Nadph Oxidases. *Med Sci (Paris)* **2006**, *22*,
36 953-9.
- 37
38 38. Pacher, P.; Beckman, J. S.; Liaudet, L. Nitric Oxide and Peroxynitrite in Health and
39 Disease. *Physiol Rev* **2007**, *87*, 315-424.
- 40
41 39. Szabo, C.; Ischiropoulos, H.; Radi, R. Peroxynitrite: Biochemistry, Pathophysiology and
42 Development of Therapeutics. *Nat Rev Drug Discov* **2007**, *6*, 662-80.
- 43
44 40. Ju, L.; Zhang, G.; Zhang, X.; Jia, Z.; Gao, X.; Jiang, Y.; Yan, C.; Duerksen-Hughes, P. J.;
45 Chen, F. F.; Li, H., *et al.* Proteomic Analysis of Cellular Response Induced by Multi-Walled
46 Carbon Nanotubes Exposure in A549 Cells. *PLoS One* **2014**, *9*, e84974.
- 47
48 41. Shen, Z. L.; Nie, H. Y.; Wang, H. F.; Yang, B.; Zhong, L. J.; Zou, X. J.; Lou, Y. X.; Liu,
49 D.; Guo, J.; Jia, G. Two Types of Mwnts with Different Surface Modifications Induce
50 Differential Expression of Proteins in Raw264.7 Cells. *Beijing Da Xue Xue Bao* **2010**, *42*, 345-
51 50.
- 52
53 42. Witzmann, F. A.; Monteiro-Riviere, N. A. Multi-Walled Carbon Nanotube Exposure
54 Alters Protein Expression in Human Keratinocytes. *Nanomedicine* **2006**, *2*, 158-68.
- 55
56 43. Haniu, H.; Matsuda, Y.; Takeuchi, K.; Kim, Y. A.; Hayashi, T.; Endo, M. Proteomics-
57 Based Safety Evaluation of Multi-Walled Carbon Nanotubes. *Toxicol Appl Pharmacol* **2010**,
58 *242*, 256-62.
- 59
60 44. Montezano, A. C.; Touyz, R. M. Mechanosensitive Regulation of Cortactin by P47phox:
A New Paradigm in Cytoskeletal Remodeling. *Circ Res* **2013**, *112*, 1522-5.
45. Shvedova, A. A.; Kisin, E. R.; Murray, A. R.; Kommineni, C.; Castranova, V.; Fadeel,
B.; Kagan, V. E. Increased Accumulation of Neutrophils and Decreased Fibrosis in the Lung of

1
2
3 Nadph Oxidase-Deficient C57bl/6 Mice Exposed to Carbon Nanotubes. *Toxicol Appl Pharmacol*
4 **2008**, 231, 235-40.

5
6 46. Elgrabli, D.; Abella-Gallart, S.; Robidel, F.; Rogerieux, F.; Boczkowski, J.; Lacroix, G.
7 Induction of Apoptosis and Absence of Inflammation in Rat Lung after Intratracheal Instillation
8 of Multiwalled Carbon Nanotubes. *Toxicology* **2008**, 253, 131-136.

9
10 47. Li, J. G.; Li, W.-X.; Xu, J.-Y.; Cai, X.-Q.; Liu, R.-L.; Li, Y.-J.; Zhao, Q.-F.; Li, Q.-N.
11 Comparative Study of Pathological Lesions Induced by Multiwalled Carbon Nanotubes in Lungs
12 of Mice by Intratracheal Instillation and Inhalation. *Environmental Toxicology* **2007**, 22, 415-
13 421.

14
15 48. Mitchell, L. A.; Gao, J.; Vander Wal, R.; Gigliotti, A.; Burchiel, S. W.; McDonald, J. D.
16 Pulmonary and Systemic Immune Response to Inhaled Multiwalled Carbon Nanotubes. *Toxicol*
17 *Sci* **2007**, 100, 203-214.

18
19 49. Shvedova, A. A.; Kisin, E. R.; Murray, A. R.; Gorelik, O.; Arepalli, S.; Castranova, V.;
20 Young, S. H.; Gao, F.; Tyurina, Y. Y.; Oury, T. D., *et al.* Vitamin E Deficiency Enhances
21 Pulmonary Inflammatory Response and Oxidative Stress Induced by Single-Walled Carbon
22 Nanotubes in C57bl/6 Mice. *Toxicol Appl Pharmacol* **2007**, 221, 339-48.

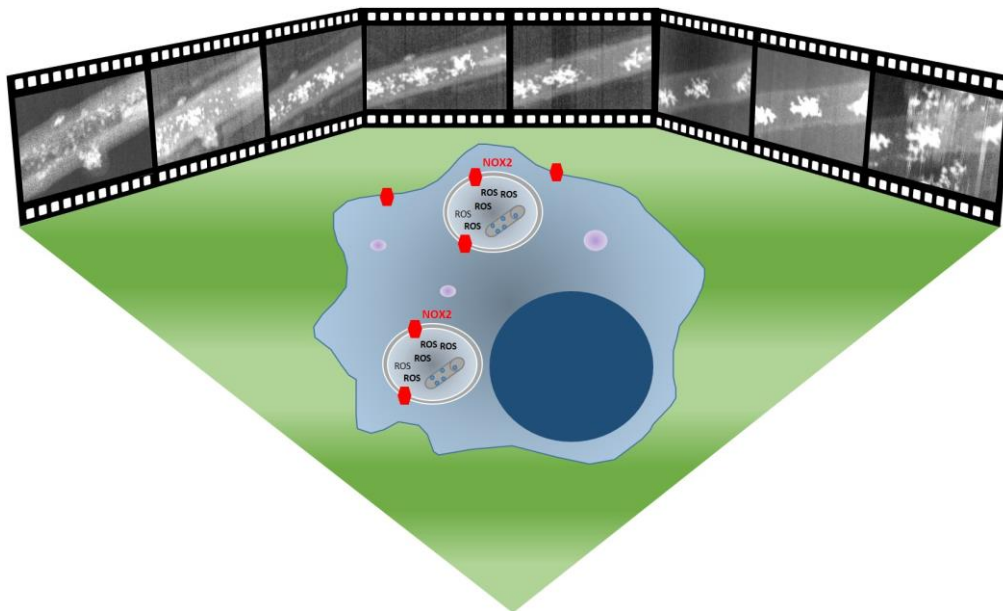
23
24 50. Baaziz, W.; Begin-Colin, S.; Pichon, B. P.; Florea, I.; Ersen, O.; Zafeiratos, S.; Barbosa,
25 R.; Begin, D.; Pham-Huu, C. High-Density Monodispersed Cobalt Nanoparticles Filled into
26 Multiwalled Carbon Nanotubes. *Chemistry of Materials* **2012**, 24, 1549-1551.

27
28 51. Baaziz, W.; Liu, X.; Florea, I.; Begin-Colin, S.; Pichon, B. P.; Ulhaq, C.; Ersen, O.;
29 Soria-Sanchez, M.; Zafeiratos, S.; Janowska, I., *et al.* Carbon Nanotube Channels Selectively
30 Filled with Monodispersed Fe₃-Xo₄ Nanoparticles. *Journal of Materials Chemistry A* **2013**, 1,
31 13853-13861.

32
33 52. Ricolleau, C.; Nelayah, J.; Oikawa, T.; Kohno, Y.; Braidy, N.; Wang, G.; Hue, F.; Florea,
34 L.; Pierron Bohnes, V.; Alloyeau, D. Performances of an 80-200 Kv Microscope Employing a
35 Cold-Feg and an Aberration-Corrected Objective Lens. *Microscopy (Oxf)* **2013**, 62, 283-93.

36
37 53. Attal, S.; Thiruvengadathan, R.; Regev, O. *Anal. Chem.* **2006**, 78, 8098-104.
38
39
40
41
42
43
44
45
46
47
48
49
50
51
52
53
54
55
56
57
58
59
60

Graphical abstract



1
2
3
4
5
6
7
8
9
10
11
12
13
14
15
16
17
18
19
20
21
22
23
24
25
26
27
28
29
30
31
32
33
34
35
36
37
38
39
40
41
42
43
44
45
46
47
48
49
50
51
52
53
54
55
56
57
58
59
60